Volume growth during uniaxial tension of particle-filled elastomers at various temperatures – Experiments and modelling

Arne Ilseng[a,b,*], Bjørn H. Skallerud[a], Arild H. Clausen[a]

[a] *Department of Structural Engineering, NTNU, Norwegian University of Science and Technology, 7491 Trondheim, Norway*
[b] *Aker Solutions AS, 3408 Tranby, Norway*

Abstract

A common presumption for elastomeric material behaviour is incompressibility, however, the inclusion of filler particles might give rise to matrix-particle decohesion and subsequent volume growth. In this article, the volumetric deformation accompanying uniaxial tension of particle-filled elastomeric materials at low temperatures is studied. An experimental set-up enabling full-field deformation measurements is outlined and novel data are reported on the significant volume growth accompanying uniaxial tension of two HNBR and one FKM compounds at temperatures of −18, 0, and 23 °C. The volumetric deformation was found to increase with reduced temperature for all compounds. To explain the observed dilatation, in situ scanning electron microscopy was used to inspect matrix-particle debonding occurring at the surface of the materials. A new constitutive model, combining the Bergström-Boyce visco-hyperelastic formulation with a Gurson flow potential function is outlined to account for the observed debonding effects in a numerical framework. The proposed model is shown to provide a good correspondence to the experimental data, including the volumetric response, for the tested FKM compound at all temperature levels.

Keywords: Elastomers, DIC, Volumetric deformation, Low temperatures, SEM, Matrix-particle debonding, Constitutive modelling

1. Introduction

Particle-filled elastomeric materials are applied in a range of industries (like automotive, aerospace, and oil and gas) where large temperature variations can occur. As a specific example, elastomeric seals can be exposed to a wide range of pressures and temperatures in subsea oil and gas equipment. As these seals are critical to avoid leakages, strict qualification testing, possibly involving temperatures from −18 to 150 °C and pressures up to 140 MPa [1], must be carried out prior to installation. The lead-time and man-hour cost of obtaining a combination of elastomeric material and seal design that would pass the qualification tests could be greatly reduced by introducing numerical analyses, like finite element simulations, into the design process. For such analyses to be

* arne.ilseng@ntnu.no

predictive and thereby cost saving, increased understanding of the underlying mechanisms occurring in elastomeric materials at various temperature and pressure levels and improved constitutive models that capture these effects are of utmost importance.

A common presumption for elastomeric material behaviour is that their deformation is fully or nearly isochoric. However, it was early shown by Gent and Park [2] and Cho et al. [3] that the inclusion of stiff filler particles, as done in nearly all industrially applied elastomer compounds, could give rise to matrix-particle debonding and subsequent volume growth. In the later years, the advances of optical measurement techniques, like digital image correlation (DIC), have facilitated accurate quantitative measurements of the possible volume strain occurring when filled elastomers are loaded in tension. Le Cam and Toussaint [4] measured the volume change accompanying uniaxial tension of filled and unfilled natural rubber specimens by the use of DIC at one surface and an assumption of material isotropy. They found a significantly larger volume growth to occur in the filled specimens. The same authors also reported significant volume growth in a filled SBR elastomer by the same experimental procedure [5]. de Crevoisier et al. [6] used two cameras for DIC measurements to capture the complete strain field during uniaxial tension of a filled SBR material, avoiding the isotropy assumption when calculating the volume change. During cyclic deformation, they found the volume growth of each cycle to start when the longitudinal strain exceeded the previously obtained maximum deformation. Cantournet et al. [7] reported the volume change of a particle filled natural rubber to depend strongly on the deformation mode. For confined and hydrostatic compression, a stiff volumetric response was reported, while matrix-particle decohesion around ZnO particles gave a more compliant volumetric behaviour in uniaxial tension. For a deformation mode dominated by hydrostatic tension, on the other hand, voids were reported to nucleate unrelated to filler particle locations. Such loading mode dependence was later echoed by Ilseng et al. [8], studying the relation between the macroscopic volume response in uniaxial tension and confined axial compression experiments and the underlying mechanism of matrix-particle decohesion. All these previous investigations on dilatation of elastomers with particles were carried out at room temperature. While the effect of temperature on the viscoelastic behaviour of elastomers is well studied in the literature [9, 10, 11, 12], it seems that the influence of temperature on the volume growth obtained in filled elastomers during uniaxial tension loading has not been given any attention yet.

Although experimental evidence shows that particle-filled elastomers might yield large volume variations in certain loading modes, constitutive models commonly used for such materials neglect this effect. For rate independent elastomeric behaviour, a range of different hyperelastic potential functions exists [13, 14, 15, 16]. In these models, a small volumetric contribution is added to the isochoric potential to include slight compressibility and ensure numerical stability, however, the large difference in volumetric behaviour between tension and compression loading in particle-filled elastomers is not accounted for. A number of models combining hyperelastic springs and strain-

rate dependent dashpots have been proposed to include also the viscous features of elastomeric materials [17, 18, 19, 20]. The visco-hyperelastic model of Bergström and Boyce [19], combining the eight-chain strain energy potential [16] with a non-linear viscous formulation, is one of the most extensively applied. However, as the volumetric behaviour of these viscous models is governed by hyperelastic potentials, they do not account for matrix-particle decohesion effects, and the stiff and fully elastic volumetric response observed in hydrostatic compression experiments on elastomeric materials [21, 22, 23] is normally used to fit their volumetric response. A few authors have proposed constitutive models that incorporate large volume growth in elastomeric materials [24, 25, 26]. Yet, the focus of these studies was on rate-independent theoretical considerations of cavitation growth for loading states of large triaxial stresses, and matrix-particle debonding during uniaxial tension was not considered. Using available constitutive models to predict the behaviour of particle-filled elastomers in loading modes dominated by positive hydrostatic stresses can cause significant errors [8], and new modelling formulations that account for a loading-mode dependent volumetric behaviour are needed.

While constitutive models that capture the effects of matrix-particle decohesion and cavitation growth on the macroscopic response have gained limited attention in the study of elastomers, it is an important area of research for ductile metallic materials. In that field, an essential piece of work, dealing with yielding of a rigid-perfectly plastic matrix containing a spherical void, was put forward by Gurson [27]. The Gurson model has subsequently been modified or extended in multiple works concerned with metallic materials [28, 29, 30, 31, 32, 33], and there are also some applications to thermoplastic polymers [34, 35, 36]. To the best of the authors' knowledge, the Gurson formulation has not yet been applied to describe the volumetric behaviour of elastomeric compounds.

In the present work, a new experimental set-up that enables DIC measurements of the complete deformation field at low temperatures is outlined. Novel data on the volume growth accompanying tension of hydrogenated nitrile butadiene rubber (HNBR) and fluoroelastomer (FKM) materials are obtained for a temperature range from -18 to 23 °C. An in situ scanning electron microscopy (SEM) study was performed at room temperature to investigate the matrix-particle debonding accompanying tension of these materials. To incorporate the volume growth in a constitutive framework, a new model is proposed by modifying the Bergström-Boyce model [19] with the use of a Gurson flow potential function [27] for the viscous behaviour.

The article is organized as follows: In the following section the set-up and experimental results for the macroscopic tension tests are outlined. Section 3 presents the set-up and the results obtained for the in situ SEM investigation. Thereafter, in Section 4, the new constitutive model including the observed viscous volume growth caused by matrix-particle debonding is presented and compared with the macroscopic experimental results. Concluding remarks are given in Section 5.

2. Macroscopic experiments

2.1. Materials

Two different HNBR compounds and one FKM material are studied herein and are in the following denoted HNBR1, HNBR2, and FKM. All three compounds are commercial materials commonly used for sealing applications in the oil and gas industry. Samples were delivered from the suppliers as dumbbell shaped specimens die stamped from 2 mm thick sheets that were obtained by a rolling process. The dimensions of the samples were in line with ISO - 37 Type 1 and Type 2 [37]. The gauge length of the Type 1 specimen used for HNBR1 is 33 mm while the gauge length of the Type 2 sample used for HNBR2 and FKM is 25 mm. The different materials, their dumbbell geometry, the gauge length, the measured pre-testing density, and the temperature range and hardness values provided by the suppliers are listed in Table 1. According to the suppliers, the lower bound of the temperature range indicates the temperature for which the materials have fully transitioned into the glassy region. As the tested compounds are commercial, their specific chemical composition cannot be disclosed.

Table 1: Tested materials, their geometries and properties

Material	Geometry	Gauge length	Density	Temperature range	Hardness
HNBR1	ISO 37 - Type 1	33 mm	1.29 g/cm^3	-35 to 150 °C	86 shore A
HNBR2	ISO 37 - Type 2	25 mm	1.19 g/cm^3	-29 to 160 °C	89 IRHD
FKM	ISO 37 - Type 2	25 mm	1.77 g/cm^3	-40 to 200 °C	89 IRHD

2.2. Set-up and data processing

The macroscopic tension experiments were performed using an Instron 5944 testing machine with a 2 kN load cell. The specimens were loaded to a machine displacement of 40 mm, and then directly unloaded until zero force was measured by the load cell. Both loading and unloading occurred at a deformation rate of 1 mm/s, which corresponds to a nominal strain rate of 0.03 s^{-1} and 0.04 s^{-1} for the Type 1 and Type 2 specimens, respectively. The same deformation procedure was applied for all temperature levels and materials, and a new specimen was used for each test. The testing was performed at temperatures of -18, 0, and 23 °C. Two tests were run for each combination of material and temperature, with the duplicates showing consistency of the reported results. Hence, one test for each combination of material and temperature will be addressed in the subsequent sections.

A custom-built temperature chamber, made of 10 mm thick transparent polycarbonate (PC) plates and connected to a supply of liquid nitrogen (LN_2), was used to obtain the low-temperature testing conditions. Stable testing temperatures were achieved by controlling the flow of LN_2 using a PID regulator. To avoid icing and condensation on the chamber walls, a tabletop fan was used to ensure sufficient air circulation around the chamber. The temperature at the specimen surface

was monitored throughout the deformation cycle by a FLIR SC7000 infrared camera, calibrated for temperatures down to -20 °C. A small rectangular hole was made in the chamber to obtain an unobstructed view between the infrared camera and the specimen. For optical deformation measurements, two Prosilica GC2450 CCD cameras were placed outside the transparent chamber. Camera 1 monitored the wide surface of the specimens, while Camera 2 monitored the thickness direction. Both cameras logged images at a frame rate of 7 Hz. As the transverse deformation of the materials tested here were shown by Ilseng et al. [8] to be anisotropic, instrumentation with two cameras is essential to obtain quantitative volume measurements. The experimental set-up is illustrated in Figure 1a, where the temperature chamber, specimen n and n+1, the two CCD cameras, the infrared camera, the tabletop fan, and the LN_2 container can be seen.

To use DIC to calculate the local deformations, a grey scale speckle pattern must be applied in the gauge section of the specimens. Ilseng et al. [12] found that the traditional use of black and white spray paint to obtain this speckle pattern was unsuited for low temperature testing, as the paint cracked during deformation. Therefore, an alternative grease-and-powder speckle was used herein. A thin layer of a Molycote 33 Medium low temperature grease was applied to the specimens gauge section, and white icing sugar was thereafter sprinkled in the greased area to create a contrast to the black specimens. A sieve with a wire mesh size of 75 µm was used to ensure a fine-grained and evenly distributed layer of the icing sugar. An example of the obtained speckle is shown in Figure 1b. Opposed to traditional spray paint, the grease and icing sugar speckle pattern did not experience cracking or other difficulties during deformation at low temperatures. The use of the PC chamber and a grease-and-powder speckle pattern was shown by Johnsen et al. [38] to yield similar results at room temperature as tests without the temperature chamber using a spray painted speckle pattern.

The frames captured by the two cameras were post-processed using the in-house DIC software *eCorr* [39]. An example of reference and deformed configuration captured with Camera 1 for a test of the HNBR1 material at -18 °C is seen in Figure 1b. For the reference frame, the initial DIC mesh is shown; while for the deformed configuration, a fringe plot of the first principal logarithmic strain is included. The logarithmic element strains in the principal directions ϵ_i^e were calculated for each element in the DIC mesh by *eCorr*, with $i = 1$ denoting the longitudinal direction and e representing the element number. Corresponding stretch ratios were found through $\lambda_i^e = \exp[\epsilon_i^e]$. A representative principal stretch ratio was obtained by calculating the mean stretch over all n elements as

$$\lambda_i = \frac{1}{n}\sum_{e=1}^{n}\lambda_i^e \tag{1}$$

and a representative logarithmic strain value was found by $\epsilon_i = \ln\lambda_i$. There was a good agreement between the representative longitudinal logarithmic strain ϵ_1 found from the two independent yet synchronized cameras [8]. Using the three representative principal stretch ratios λ_i, the volume

ratio J was calculated as

$$J = \lambda_1 \lambda_2 \lambda_3 \tag{2}$$

while the longitudinal Cauchy stress was found from

$$\sigma_1 = \frac{F}{A} = \frac{F}{\lambda_2 \lambda_3 A_0} \tag{3}$$

where F is the force measured by the load cell, A the current cross sectional area, A_0 the initial cross sectional area, and λ_2 and λ_3 are the transverse stretch ratios. For the uniaxial tension tests ($\sigma_2 = \sigma_3 = 0$), the hydrostatic stress is defined as

$$\sigma_H = \frac{\sigma_1}{3} \tag{4}$$

Finite element simulations of the thermal conditioning process, using the material parameters and the numerical procedure outlined by Ilseng et al. [12], showed that 8 minutes of thermal conditioning should be sufficient to cool the centre of the sample from room temperature to nearly -18 °C. During the experimental testing, specimen n+1 was placed in the temperature chamber for cooling at the same time as sample n was mounted in the testing machine. Moreover, a 10-minute conditioning period was included between mounting a sample in the machine and the start of the deformation cycle. During this period, the machine was set to retain zero force in the load cell to account for thermal contraction of the specimen. Before the first test at a new temperature level, a 30-minute tempering period was included to ensure sufficient cooling of the steel grips of the testing machine.

2.3. Results

2.3.1. Stress - strain

The Cauchy stress - logarithmic strain behaviour in the longitudinal direction of the three materials is shown in Figure 2. As expected, a clear increase of stiffness and strength for the loading process can be seen to take place for all materials as the temperature is reduced. During unloading, however, the temperature had limited influence on the material response. The significant dip in stress level seen to occur at a strain of about 0.4 in the HNBR1 material at low temperatures was previously discussed by Ilseng et al. [12], where brittle matrix-particle debonding was suggested as a plausible physical mechanism. It can be noted that the slight wobbling in the loading curve for the HNBR2 and the FKM materials at -18 °C coincided with the injection of liquid nitrogen into the chamber, and was likely caused by small temperature variations in the specimens.

2.3.2. Volume growth

The volume ratio vs longitudinal logarithmic strain data are shown for all materials and temperatures in Figure 3. For the large strain regime, a clear trend is that the volumetric deformation increases as the temperature is reduced, leading to a significant maximum volume growth at low temperatures for all three compounds, although somewhat more modest for the HNBR2 material

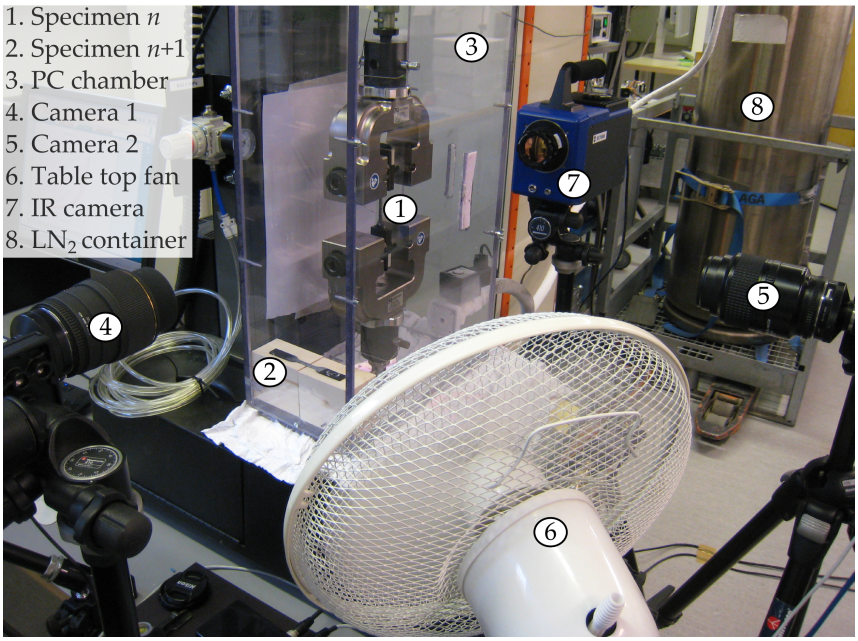

(a)

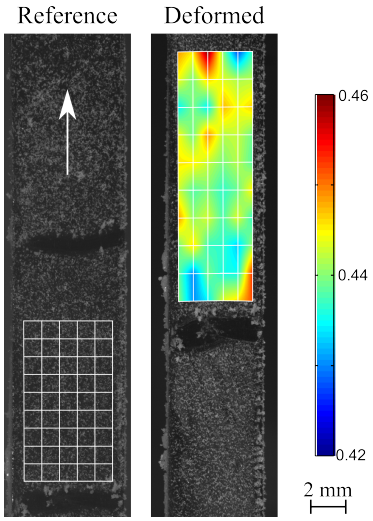

(b)

Figure 1: (a) Experimental set-up used in the macroscopic tension experiments, (b) DIC frames from Camera 1 for a test on HNBR1 at $-18\,^{\circ}\mathrm{C}$. The white arrow on the reference configuration indicates tension direction, while the black horizontal lines in the speckle pattern were used to match the location of the mesh between images from Camera 1 and Camera 2. The fringe plot indicates the value of the first principal logarithmic strain. A 2 mm bar is included for scale.

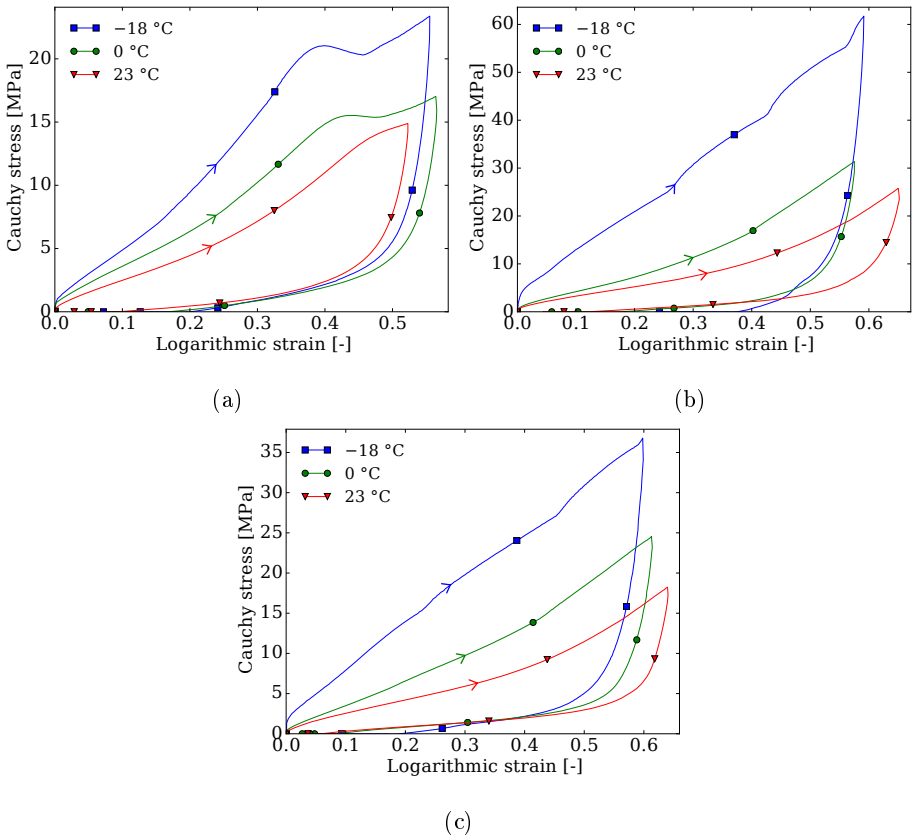

Figure 2: Longitudinal Cauchy stress - logarithmic strain data for all three temperatures (a) HNBR1, (b) HNBR2, and (c) FKM. Arrows indicate the direction of the loading cycle.

compared with the two other ones. In addition, all materials show a volume ratio close to unity at low strains, while the volume increase sets on after a critical strain level is reached. This behaviour is in line with a matrix-particle debonding theory, where a certain amount of strain/stress would be needed for the bonding between the matrix and the particles to break, and thereby the volume to start increasing. In general, the obtained critical strain level is lowered as the temperature is reduced.

The onset of volume growth for the HNBR1 material, as illustrated in Figure 3a, is observed to coincide with the stress dip seen in Figure 2a, supporting a theory of brittle matrix-particle debonding at low temperatures. In addition, a clear loop in the loading-unloading behaviour can be seen for this compound, with the volume ratio being clearly larger for the same strain level during unloading compared with loading. Further, the maximum volume growth of the HNBR1 material is strongly temperature dependent, with the volume variation being only a few percent at 23 °C, while more than 20 % volume growth was obtained for the test at −18 °C. The results for the HNBR2 material presented in Figure 3b display virtually no volume change at room temperature. However, as the temperature decreases, a clear volume growth can be observed in the large deformation regime. In the FKM results, on the other hand, presented in Figure 3c, more than 20 % volume increase is seen at all three temperatures. For this material the volume

ratio - logarithmic strain response is relatively similar for the 23 and 0 °C tests, while the volume change at −18 °C is distinctively larger, with a maximum value of 28 % volume growth. Clearly, the common assumption of isochoric behaviour of elastomeric materials is not valid for the tested compounds, especially not at low temperatures.

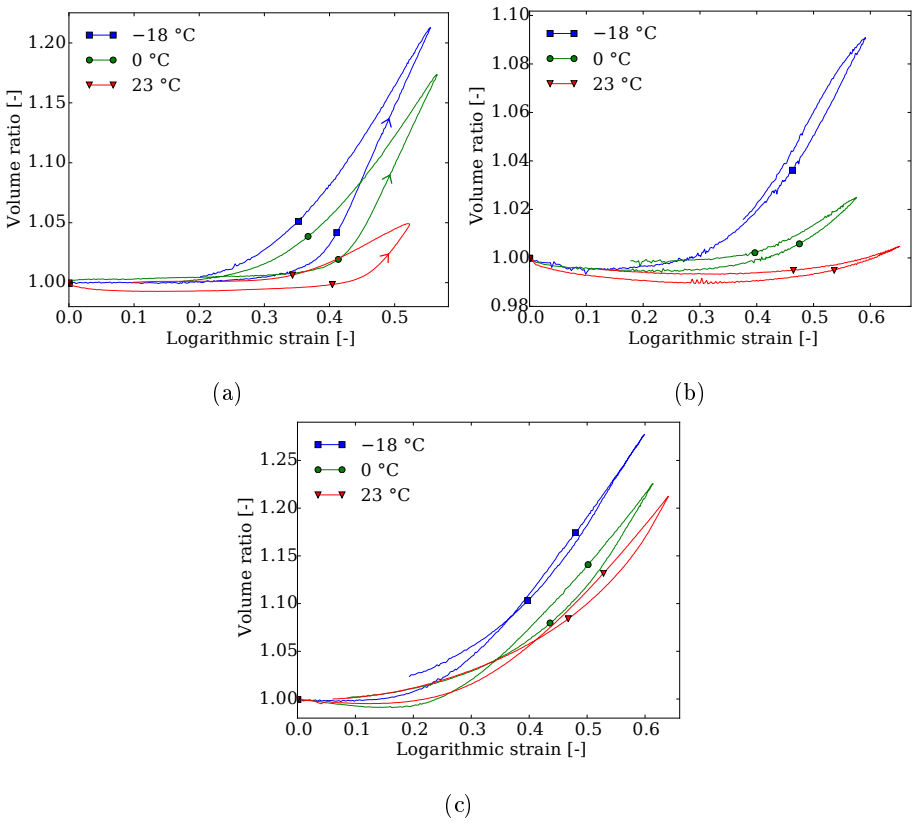

Figure 3: Volume ratio - logarithmic strain data for all three temperatures (a) HNBR1, (b) HNBR2, and (c) FKM. Arrows in (a) indicate the direction of the loading cycle.

To obtain a continuum based constitutive model that accounts for the observed volume growth in elastomers, the relation between the hydrostatic stress and the volume ratio, as shown in Figure 4, is essential. For all materials, a critical stress level is seen to be needed before the volume growth sets on, corresponding to the critical strain level illustrated in Figure 3. This critical stress appears to increase with decreasing temperature, while the slope of the curves after the volume increase has started is nearly equal for all temperature levels. A clear hysteresis loop is apparent for all materials at all temperatures, indicating a viscous volumetric behaviour. As the volume returns to its initial value for the 0 and 23 °C tests, the process is assumed viscoelastic. For the HNBR1 material in Figure 4a there is a clear plateau level where the volume increases significantly for a nearly constant hydrostatic stress value. The stress associated with this plateau corresponds to the onset of the dip in the stress-strain curve seen in Figure 2a. Compared to the loading process, the response during unloading is seen to be less sensitive to the temperature level, as illustrated by the FKM material at 0 and 23 °C for which the unloading curves coincide. For most curves, a

slight volume reduction can be seen during the initial part of the test. At such small deformations, there might be inaccuracies in the DIC measurements.

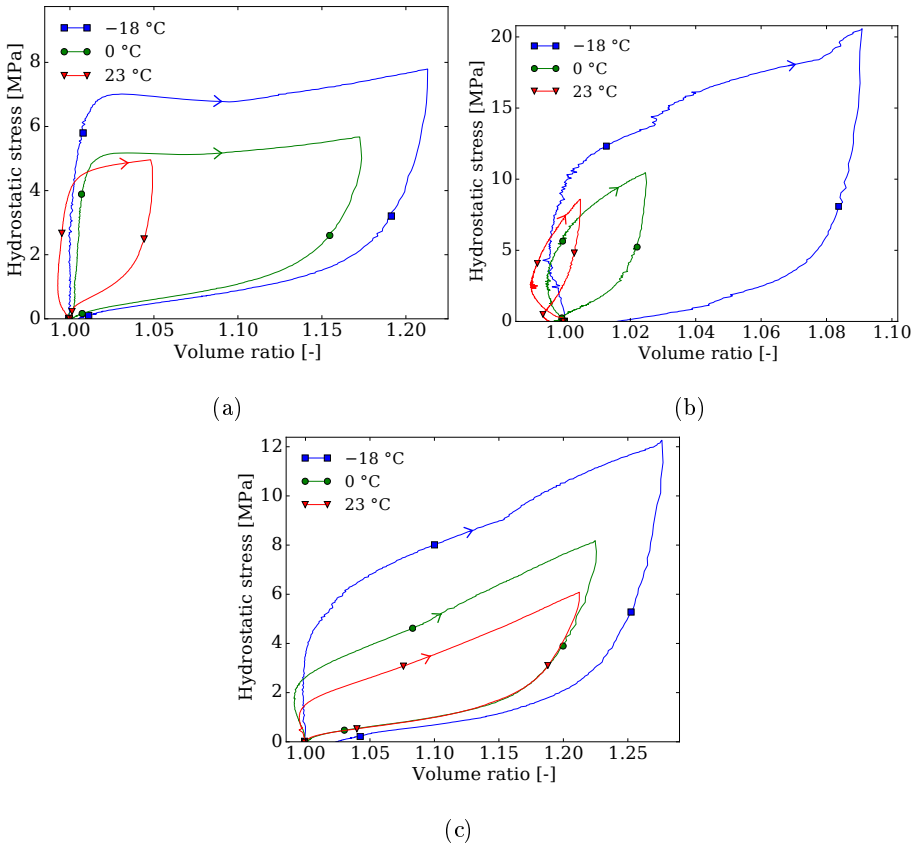

Figure 4: Hydrostatic stress - volume ratio data for all three temperatures (a) HNBR1, (b) HNBR2, and (c) FKM. Arrows indicate the direction of the loading cycle.

2.3.3. Temperature change

The maximum temperature increase in the deformation cycle, measured at the surface of the materials by the infrared camera, is shown for all tests in Figure 5. The temperature change increased for colder testing conditions for all materials, as to be expected from the enlarged hysteresis loops obtained at low temperatures in the stress - strain plots of Figure 2. The high stress levels at reduced temperatures may also explain why the largest increase of temperature occurs at −18 °C. The greatest temperature change was found for the HNBR2 material tested at −18 °C, which experienced a temperature increase of 9 °C at its surface.

3. In situ SEM experiments

3.1. Motivation

A possible micromechanical explanation for the significant dilatation accompanying tension deformation of the tested materials is that debonding between the matrix material and filler particles leads to cavities and thereby macroscopic volume growth [2, 3]. If this hypothesis is correct,

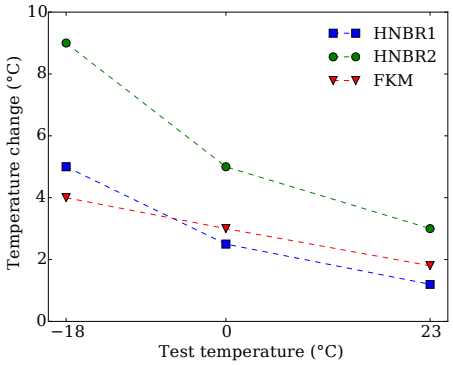

Figure 5: Maximum temperature increase at the surface of the samples during deformation for all materials and test temperatures.

micrographs of such debonding should be feasible to obtain by in situ SEM. Therefore, the two compounds HNBR1 and FKM, showing clear volume growth for the macroscopic tension tests at room temperature, were investigated by in situ SEM.

It should be mentioned that a drawback of using SEM is that it only gives indications of debonding at the surface of the materials. An in situ X-ray tomography study (see e.g. [40]) that could give information on debonding and cavity growth in the inner part of the specimens would therefore be favourable, however, the necessary equipment for in situ tomography studies is not available to the authors. The full SEM study and its results are discussed in length by Ilseng et al. [8], however, a brief presentation is given here for completeness.

3.2. Set-up

A purpose-built tension rig [41] was placed on the sample board of a Zeiss Gemini Ultra 55 Limited Edition SEM apparatus to obtain the in situ micrographs. A photo of the tension rig can be seen in Figure 6a. Small tension specimens, having dimensions in line with the sketch in Figure 6b, were cut from the ISO geometry specimens delivered by the suppliers. The materials were tested at room temperature, and deformed at a nominal strain rate of 0.01 s^{-1} until a nominal stretch of 2 was reached. The outer surface of the gauge section of the stretched specimens (9×3 mm^2 area in Figure 6b) were studied by SEM using a random walk procedure where micrographs were captured at locations of interest with a resolution of 3072×2072 pixels.

3.3. Results

Using energy-dispersive X-ray spectroscopy (EDS), both materials were found to contain a significant number of ZnO particles [8], a type of inclusion previously reported to be prone to debonding [7, 42, 43]. For the HNBR1 material, decohesion between the matrix material and ZnO particle inclusions was observed at multiple locations, as illustrated by the two marked particles in Figure 7a (more micrographs displaying matrix-particle debonding for the HNBR1 material can be found in [8]). For the FKM compound, on the other hand, the conductive properties

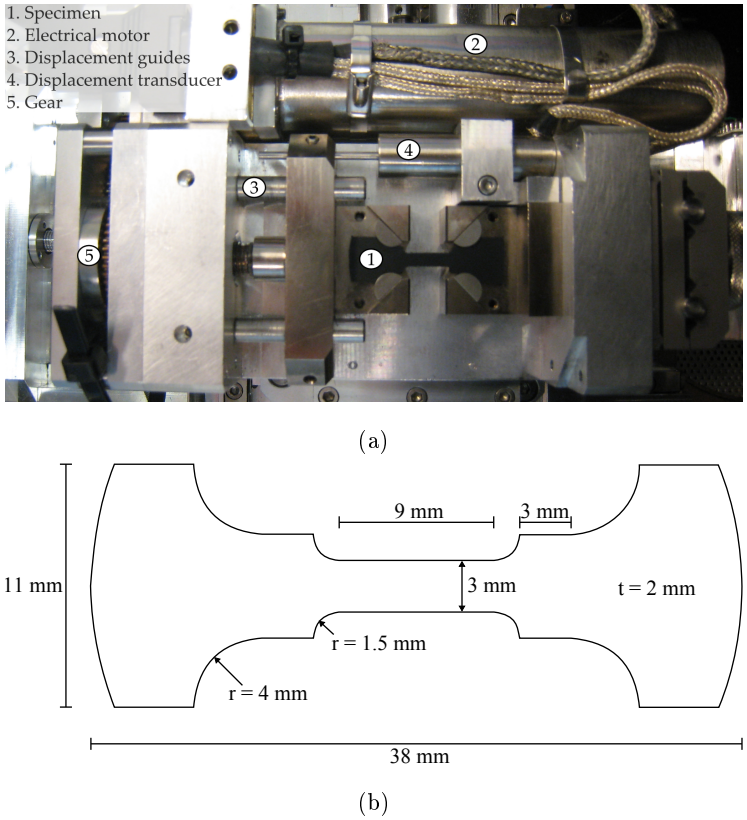

Figure 6: Set-up for the in situ SEM study, (a) test specimen in tension rig, and (b) geometry of in situ specimens cut from the ISO dimension samples [8].

of the material were challenging in the deformed configuration, leading to low contrast in the obtained micrographs. However, indication of matrix-particle debonding could be found also for this material, as illustrated in Figure 7b.

The findings of the SEM study support the theory that the main source for the macroscopic volume growth is that of matrix-particle decohesion. Consequently, it is believed that the thermal sensitivity of the volumetric response of the materials in uniaxial tension showed in Section 2.3.2 is caused by a temperature dependent behaviour of the cohesive zone between the matrix material and the filler particles.

4. Constitutive modelling

4.1. Preliminaries

From the experimental results presented in Section 2 and 3 it is clear that significant volume increase, partly or solely caused by matrix-particle debonding, can accompany tension of particle-filled elastomeric materials, and that this volume growth gets more pronounced as the temperature is reduced. It was also shown that a threshold value for the hydrostatic stress has to be reached before any significant increase of volume takes place. In addition, a significant hysteresis in the hydrostatic stress - volume ratio behaviour was observed. In this section, a new constitutive model,

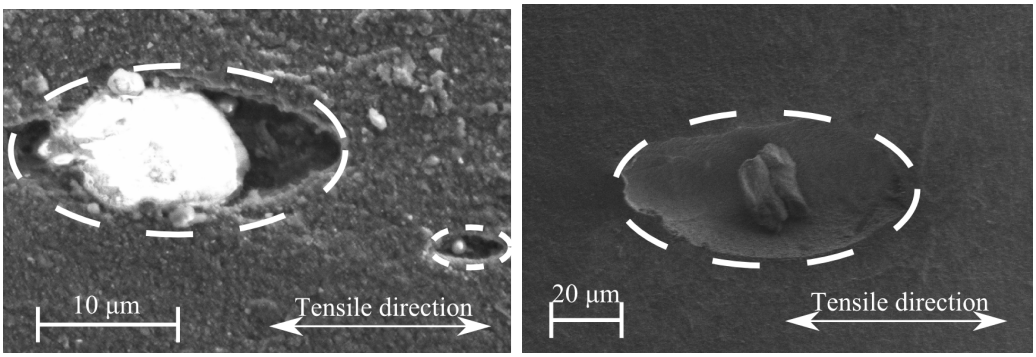

(a) (b)

Figure 7: Debonding observed at a nominal longitudinal stretch of 2 for (a) HNBR1 and (b) FKM. Cavities are indicated by dashed white lines.

combining the visco-hyperelastic Bergström-Boyce model [19] with the Gurson flow potential function [27], is outlined to capture the experimental observations. While the behaviour of the tested compounds is known to be slightly anisotropic [8], having important consequences for the experimental setup, the concepts and ideas of capturing the viscous volume growth in the proposed model is better conveyed using a simplified isotropic modelling procedure. Including anisotropic effects in the model is therefore left for further work, and an isotropic framework is used in the following presentation.

To introduce the notation used in this section, a brief summary of important continuum mechanical concepts is included. For a thorough review, the reader is referred to the textbooks by Holzapfel [44] or Belytschko et al. [45]. The main kinematic variable of continuum mechanics is the deformation gradient $\mathbf{F}$, and this tensor is defined by

$$\mathbf{F} = \frac{\partial \boldsymbol{x}}{\partial \boldsymbol{X}} \tag{5}$$

where $\boldsymbol{x}$ is a particle position in the current configuration, and $\boldsymbol{X}$ is the position of the same particle in the reference configuration. Further, the left and right Cauchy-Green deformation tensors, $\mathbf{b}$ and $\mathbf{C}$ respectively, are defined as

$$\mathbf{b} = \mathbf{F}\mathbf{F}^T, \quad \mathbf{C} = \mathbf{F}^T\mathbf{F} \tag{6}$$

while the volume ratio J can be found from

$$J = \mathrm{det}\mathbf{F} \tag{7}$$

Purely distortional parts of the Cauchy-Green deformation tensors are found through

$$\mathbf{b}^* = J^{-2/3}\mathbf{b}, \quad \mathbf{C}^* = J^{-2/3}\mathbf{C} \tag{8}$$

The deviatoric part of a tensor $\mathbf{A}$ is calculated as

$$\mathbf{A}' = \mathbf{A} - \left(\frac{1}{3}\mathrm{tr}\mathbf{A}\right)\mathbf{I} \tag{9}$$

where $\mathbf{I}$ is the second order unit tensor. The first invariant of the full and the distortional left and right Cauchy-Green tensors is

$$I_1 = \mathrm{tr}\mathbf{b} = \mathrm{tr}\mathbf{C}, \quad I_1^* = \mathrm{tr}\mathbf{b}^* = \mathrm{tr}\mathbf{C}^* \tag{10}$$

4.2. Model formulation

The proposed model consists of two parallel parts having a hyperelastic spring in Part A and a non-linear viscous dashpot in series with a hyperelastic spring in Part B, as illustrated by the rheological 1D representation in Figure 8. The deformation gradient tensors of Part A and Part B is by definition equal to the total deformation gradient

$$\mathbf{F} = \mathbf{F}_\mathrm{A} = \mathbf{F}_\mathrm{B} \tag{11}$$

while the total Cauchy stress tensor is the sum of the stresses in Part A and Part B

$$\boldsymbol{\sigma} = \boldsymbol{\sigma}_\mathrm{A} + \boldsymbol{\sigma}_\mathrm{B} \tag{12}$$

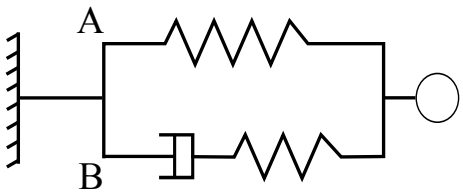

Figure 8: 1D rheological representation of the constitutive model.

4.2.1. Part A

As in the Bergström-Boyce model [19], the elastic spring in Part A is governed by the eight-chain Arruda-Boyce potential function [16] for the deviatoric part combined with a volumetric potential function as used by Simo and Miehe [46]. The Cauchy stress tensor then reads

$$\boldsymbol{\sigma}_\mathrm{A} = \frac{\mu_\mathrm{A}\lambda_L}{3J_\mathrm{A}\lambda_\mathrm{A}^*}\mathcal{L}^{-1}\left(\frac{\lambda_A^*}{\lambda_L}\right)(\mathbf{b}_\mathrm{A}^*)' + \frac{\kappa_\mathrm{A}}{2}\left(J - \frac{1}{J}\right)\mathbf{I} \tag{13}$$

where μ_A is the effective shear modulus, κ_A the effective bulk modulus, λ_L the locking stretch, J is the volume ratio for the spring in Part A found from $J = \det\mathbf{F}_\mathrm{A} = \det\mathbf{F}$, and $\mathcal{L}^{-1}$ is the inverse Langevin function, with the Langevin function being defined by $\mathcal{L}(x) = \coth(x) - 1/x$. For the Fortran implementation of the model, the inverse Langevin function was solved by Newton's method, using a Padé approximation [47] for the initial guess. The effective stretch λ_A^* is defined as

$$\lambda_\mathrm{A}^* = \sqrt{\frac{1}{3}\mathrm{tr}\mathbf{b}_\mathrm{A}^*} \tag{14}$$

4.2.2. Part B

Kinematics. The deformation gradient of Part B is decomposed multiplicatively in an elastic and a viscous part [48], as illustrated in Figure 9

$$\mathbf{F}_{\mathrm{B}} = \mathbf{F}_{\mathrm{B}}^{e}\mathbf{F}_{\mathrm{B}}^{v} \tag{15}$$

This leads to a multiplicative split in elastic and viscous parts also for the volume ratio of Part B

$$J_{\mathrm{B}} = J_{\mathrm{B}}^{e}J_{\mathrm{B}}^{v} \tag{16}$$

The viscous velocity gradient defined on the intermediate configuration $\tilde{\Omega}$, see Figure 9, can be found as

$$\tilde{\mathbf{L}}_{\mathrm{B}}^{v} = \dot{\mathbf{F}}_{\mathrm{B}}^{v}\left(\mathbf{F}_{\mathrm{B}}^{v}\right)^{-1} = \tilde{\mathbf{D}}_{\mathrm{B}}^{v} + \tilde{\mathbf{W}}_{\mathrm{B}}^{v} \tag{17}$$

where $\tilde{\mathbf{D}}_{\mathrm{B}}^{v}$ is the symmetric rate-of-deformation tensor and $\tilde{\mathbf{W}}_{\mathrm{B}}^{v}$ the anti-symmetric spin tensor. Due to material isotropy, one can obtain that $\tilde{\mathbf{W}}_{\mathrm{B}}^{v} = \mathbf{0}$ and a relation for $\tilde{\mathbf{D}}_{\mathrm{B}}^{v}$ can be defined

$$\tilde{\mathbf{D}}_{\mathrm{B}}^{v} = \dot{\Lambda}\mathbf{N}_{\mathrm{B}}^{v} \tag{18}$$

where $\dot{\Lambda}$ denotes a viscous multiplier. The direction of the viscous deformation is denoted $\mathbf{N}_{\mathrm{B}}^{v}$, and can be found as the gradient of a flow potential function g according to

$$\mathbf{N}_{\mathrm{B}}^{v} = \frac{\partial g}{\partial \tilde{\mathbf{\Sigma}}_{\mathrm{B}}} \tag{19}$$

where $\tilde{\mathbf{\Sigma}}_{\mathrm{B}}$ is the Mandel stress tensor, defined on the intermediate configuration and related to the Cauchy stress $\boldsymbol{\sigma}_{\mathrm{B}}$ by

$$\tilde{\mathbf{\Sigma}}_{\mathrm{B}} = J_{\mathrm{B}}^{e}\left(\mathbf{F}_{\mathrm{B}}^{e}\right)^{T}\boldsymbol{\sigma}_{\mathrm{B}}\left(\mathbf{F}_{\mathrm{B}}^{e}\right)^{-T} \tag{20}$$

By combining Equation 17 and 18, a rate equation for the viscous deformation gradient can be obtained as

$$\dot{\mathbf{F}}_{\mathrm{B}}^{v} = \dot{\Lambda}\mathbf{N}_{\mathrm{B}}^{v}\mathbf{F}_{\mathrm{B}}^{v} \tag{21}$$

Elastic spring. An eight-chain model simular to the one in Part A, but formulated on the intermediate configuration $\tilde{\Omega}$ is used for the spring in Part B

$$\tilde{\mathbf{\Sigma}}_{\mathrm{B}} = \frac{\mu_{\mathrm{B}}\lambda_{L}}{3\lambda_{\mathrm{B}}^{e*}}\mathcal{L}^{-1}\left(\frac{\lambda_{\mathrm{B}}^{e*}}{\lambda_{L}}\right)\left(\tilde{\mathbf{C}}_{\mathrm{B}}^{e*}\right)' + \frac{\kappa_{\mathrm{B}}}{2}\left(\left(J_{\mathrm{B}}^{e}\right)^{2} - 1\right)\mathbf{I} \tag{22}$$

where μ_B is the shear modulus of the spring, κ_B is the bulk modulus, and $\lambda_{\mathrm{B}}^{e*} = \sqrt{\frac{\mathrm{tr}\mathbf{C}_{\mathrm{B}}^{e*}}{3}}$.

Dashpot. The flow potential g, used to obtain the direction of the viscous deformation of the dashpot in line with Equation 19, is defined by the Gurson yield function [27] to incorporate the effects of matrix-particle decohesion

$$g = \left(\frac{\sigma_{eq}}{\bar{\sigma}}\right)^{2} + 2q_{1}f\cosh\left(\frac{q_{2}\mathrm{tr}\tilde{\mathbf{\Sigma}}_{\mathrm{B}}}{2\bar{\sigma}}\right) - \left(1 + q_{3}f^{2}\right) \tag{23}$$

where f is the void fraction, $\bar{\sigma}$ is a normalizing stress, q_i are the material parameters introduced in the model by Tvergaard [28], while σ_{eq} is the equivalent stress defined by the relation

$$\sigma_{eq} = \sqrt{\frac{3}{2}\tilde{\mathbf{\Sigma}}'_{\mathrm{B}} : \tilde{\mathbf{\Sigma}}'_{\mathrm{B}}} \tag{24}$$

The direction of the viscous deformation can then be obtained as

$$\mathbf{N}^v_{\mathrm{B}} = \frac{\partial g}{\partial \tilde{\mathbf{\Sigma}}_{\mathrm{B}}} = \frac{q_1 q_2 f}{\bar{\sigma}} \sinh\left(\frac{q_2 \mathrm{tr}\tilde{\mathbf{\Sigma}}_{\mathrm{B}}}{2\bar{\sigma}}\right)\mathbf{I} + \frac{3}{\bar{\sigma}^2}\tilde{\mathbf{\Sigma}}'_{\mathrm{B}} = n_{vol}\mathbf{I} + n_{dev}\tilde{\mathbf{\Sigma}}'_{\mathrm{B}} \tag{25}$$

It is emphasized that the Gurson potential is solely used to define the direction of the viscous flow and not as a traditional yield criterion.

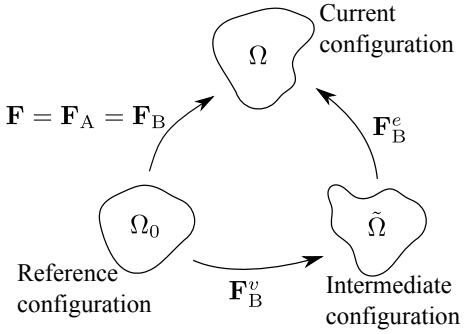

Figure 9: Illustration of the multiplicative decomposition of the deformation gradient.

Finally, one needs to establish a constitutive equation for the viscous behaviour. The most common way of doing this is by defining a constitutive law for an effective viscous strain rate measure. However, as the viscous multiplier does not coincide with an effective viscous strain rate measure in the presented model, a relation between the two would be needed to obtain the viscous multiplier to be used in Equation 21. Consequently, instead of going through an effective viscous strain rate, a constitutive equation is here defined directly for the viscous multiplier as it makes it easier to connect the model formulation and the simulation results.

The critical stress/strain level where the volume growth was seen to set on in the experimental tests can be included in the constitutive model for the viscous multiplier in two different ways; (i) a strongly non-linear viscous behaviour would ensure that the volume growth is negligible during the initial part of the deformation; (ii) a critical stress level could be introduced in the calculation of the viscous multiplier to ensure no viscous deformation before the critical stress level is reached. As there is no experimental data available on how the critical stress level potentially evolves with strain rate, we here choose the first method for simplicity. Introducing an explicit critical stress and defining its relation to strain rate is for the time left for further work. To obtain a strongly non-linear viscous behaviour a power law expression is used as the constitutive relation for the viscous multiplier $\dot{\Lambda}$ in line with the original Bergström-Boyce model [19]

$$\dot{\Lambda} = \dot{\Lambda}_0 \left(\frac{\sqrt{\tilde{\mathbf{\Sigma}}_{\mathrm{B}} : \tilde{\mathbf{\Sigma}}_{\mathrm{B}}}}{f_v \bar{\tau}}\right)^m \tag{26}$$

where $\dot{\Lambda}_0$ is included to ensure dimensional consistency by defining it as 1 Pa/s (as the unit of $\mathbf{N}_{\mathrm{B}}^{v}$ is 1/Pa), while $\bar{\tau}$ is a material parameter representing a scaling stress. The coefficient f_v is introduced to incorporate the difference in the strain rate sensitivity between loading and unloading, and is defined as [49]

$$f_v = 1 + \alpha \boldsymbol{\epsilon} : \boldsymbol{\epsilon}^e \tag{27}$$

where α is a material parameter, $\boldsymbol{\epsilon} = \ln[\mathbf{V}]$, and $\boldsymbol{\epsilon}^e = \ln[\mathbf{V}^e]$, with $\mathbf{V}$ being the left stretch tensor defined as $\mathbf{V}^2 = \mathbf{b}$, and correspondingly $(\mathbf{V}^e)^2 = \mathbf{b}_{\mathrm{B}}^e$. The exponent m in Equation 26 is a material parameter that, since f_v theoretically can be negative, is set to be an even positive integer to ensure that $\dot{\Lambda} \geq 0$ for any deformation. This combined with the convexity of the Gurson potential function ensures non-negative dissipation (i.e. $\tilde{\boldsymbol{\Sigma}}_{\mathrm{B}} : \tilde{\mathbf{D}}_{\mathrm{B}}^{v} \geq 0$). It can be noted that the full Mandel stress tensor is used in Equation 26, as opposed to only the deviatoric part as in the original Bergström-Boyce model [19]. This is done to ensure that viscous volume growth is obtained also for a pure hydrostatic tension loading, as to be expected from the matrix-particle decohesion theory. In addition, a purely stress-activated viscous deformation is employed, neglecting the deformation-induced viscosity in the original model, as it improved the fit between the model and the experimental results.

The initial particle fraction f_0 is an input parameter to the model, while an evolution equation for the void fraction defined from conservation of mass, assuming that the volume fraction of voids can only increase due to growth of cavities around filler particles and not through void nucleation, reads

$$\dot{f} = (1 - f)\,\mathrm{tr}\tilde{\mathbf{D}}_{\mathrm{B}}^{v} = (1 - f)\left(3\dot{\Lambda} n_{vol}\right) \tag{28}$$

where n_{vol} was defined in Equation 25. As the filler particles in the HNBR1 and FKM materials were made of ZnO, which is known to be nearly rigid compared with the stiffness of the elastomeric matrix, the void fraction f is set to be equal or greater than its initial level f_0 at all times, i.e. the particles cannot be compressed. This is included in the model through the steps of Algorithm 1.

Algorithm 1: Procedure to ensure $f \geq f_0$ in iteration step n+1 with time increment dt

Input from step n: $(I_{1B})_n$, f_n, $\dot{\Lambda}_n$

$n_{dev} = \frac{3}{\bar{\sigma}^2}$

$n_{vol} = \frac{q_1 q_2 f_n}{\bar{\sigma}} \sinh\left(\frac{q_2 (I_{1\mathrm{B}})_n}{2\bar{\sigma}}\right)$

$\dot{f} = (1 - f_n)\, 3\dot{\Lambda}_n n_{vol}$

$f_{n+1} = f_n + dt\dot{f}$

if $f_{n+1} < f_0$ **then**

  $f_{n+1} = f_0$

  $n_{vol} = 0$

end

$\mathbf{N}_B^v = n_{vol}\mathbf{I} + n_{dev}\tilde{\boldsymbol{\Sigma}}'_B$

4.3. Temperature dependence

For the thermal modelling of the materials, the relatively small deformation-induced temperature increase addressed in Figure 5 is neglected, limiting the simulations to isothermal conditions. Consequently, the temperature dependence can be included in the model solely by defining the material parameters as functions of the testing temperature [50]. A simple mathematical relation was applied to all temperature dependent parameters, defined for a dummy parameter a as [51]

$$a\left(\theta\right) = a_0 \exp\left[\frac{\theta_0 - \theta}{\theta_{base}}\right] \tag{29}$$

where θ is the testing temperature, a_0 the parameter value at $\theta_0 = 296$ K, and θ_{base} a scaling temperature. The expression in Equation 29 is purely empirical and improving the model with a more physical relation to temperature and accounting for non-isothermal conditions (see e.g. [9, 50, 52]) is left for further work.

4.4. Determination of material parameters

To illustrate the capabilities of the proposed model at the three testing temperatures, the behaviour of the FKM material was simulated as this compound displayed the largest volume variations. The optimization software LS-OPT [53] was used to obtain the temperature dependent parameters, resulting in the values listed in Table 2. The remaining model parameters were defined as temperature independent, and their values are listed in Table 3. The bulk modulus $\kappa_B = 2.2$ GPa was found from confined axial compression experiments on similar materials [8], while the values $m = 6$, $\lambda_L = 1.8$, and $\alpha = 50$ yielded reasonable agreement between simulation and experimental results for all temperature levels. The same locking stretch was used for the springs in Part A and Part B. Since $\dot{\Lambda}_0$ was included in Equation 26 only for dimensional consistency, its value was set to unity. For the parameters q_1 and q_2, the same values as proposed by Tvergaard [28], being 1.5 and 1 respectively, were used (note that q_3 in Equation 23 is not present in the model due to the differentiation in Equation 25). The initial particle volume fraction f_0 was set to 0.01 based on the pre-deformation SEM images presented by Ilseng et al. [8].

It should be noted that experimental data at different loading rates are not available for the studied materials, and the parameters for the viscous response of the model are thereby fitted to data for one strain rate only. Consequently, pronounced uncertainty is related to the optimized values for these parameters, and they should not be expected to yield predictive results for other deformation rates. However, the obtained parameters are considered sufficient for illustrating the qualitative capabilities of the proposed model. It is left for further work to get experimental data for a range of strain rates and do a subsequent evaluation of how the constitutive model captures the material behaviour at various strain rates.

4.5. Results

The constitutive model was implemented in Fortran as an explicit user-defined material model for the commercial finite element software LS-DYNA [54], and was tested on an 8-node brick ele-

Table 2: Optimized a_0 and θ_{base} values of Equation 29 for temperature dependent parameters to fit the behaviour of the FKM material.

	a_0	θ_{base}
μ_A	1.33 MPa	41.7 K
κ_A	24.0 MPa	134.0 K
μ_B	17.20 MPa	27.7 K
$\bar{\sigma}$	0.40 MPa	31.1 K
$\bar{\tau}$	0.63 MPa	33.8 K

Table 3: Temperature independent variables used for the FKM material.

κ_B	m	λ_L	α	$\dot{\Lambda}_0$	q_1	q_2	f_0
2.2 GPa	6	1.8	50	1 Pa/s	1.5	1	0.01

ment. The loading was defined by applying the stress-time history obtained in the FKM experiment at the corresponding testing temperature to one face of the element.

The Cauchy stress - logarithmic strain and hydrostatic stress - volume ratio results from the proposed model are compared with the experimental data for the three temperature levels in Figure 10a and Figure 10b, respectively. In general, a good agreement between experimental and simulation results is obtained, and the temperature dependence of the response is well captured by the simple relation used in the model.

For the stress - strain response in Figure 10a, a reasonably good fit between the model and the experimental data is seen, although a too compliant response is obtained in the 23 °C simulation, leading to an overestimation of the maximum deformation. For the 0 and −18 °C simulations, on the other hand, the initial stiffness is seen to be too high, exaggerating the stress response at small strains. In addition, the strain level at the end of the unloading is larger in the simulation results than in the experimental data.

Looking closer at the hydrostatic stress - volume ratio results in Figure 10b, the qualitative features of a temperature dependent critical stress level and a clear hysteresis loop are represented reasonably accurate by the model. In general, the loading behaviour of the simulations conforms well to the experimental data, while the predicted volume ratios are decreasing too slowly during the initial phase of unloading. Moreover, as for the strain level, the predicted volume ratios at the end of the deformation cycles are too large compared with the experimental data.

The evolution of the void fraction f with hydrostatic stress is shown in Figure 10c for all three simulations. Due to the viscous multiplier's non-linear dependence on the stress level, f grows at a negligible rate in the first part of the simulation before it starts to increase rapidly with increasing hydrostatic stress. It is observed that the hydrostatic stress at which f starts to grow coincides well with the stress where the volume ratio departed from 1 in Figure 10b. Then again,

during the initial decrease of the hydrostatic stress f is nearly constant. The upper plateaus of the curves in Figure 10c correspond with the initially slow decrease of the volume ratios in Figure 10b. The explanation for this behaviour can be found from the gradient component n_{vol} of Equation 25 and the viscous multiplier $\dot{\Lambda}$. As the material starts to unload, the hydrostatic stress in the spring of Part B goes from tension to compression, yielding a low value of n_{vol} and $\dot{\Lambda}$ during this transition. Consequently, the changes of the volumetric part of the viscous deformation gradient tensor (Equation 21) and the void volume fraction (Equation 28) are small during the initial phase of unloading.

The ratio between the two bulk moduli of the model, κ_A and κ_B, deserves some further attention. The fact that $\kappa_A << \kappa_B$ ensures that nearly all volumetric deformation in Part B occurs in the dashpot during uniaxial tension, making the volumetric increase visco-hyperelastic. When, on the other hand, the model is subjected to negative hydrostatic stress situations, the requirement of $f \geq f_0$ suppresses the dashpot from deforming volumetrically, and the stiff rate-independent volumetric response of the spring in Part B is dominating the overall behaviour, matching observations from experimental work [8]. This is illustrated in Figure 10d, where the model's response to a volumetric compression is compared with experimental results from confined axial compression tests on FKM at room temperature [8]. Wood and Martin [22] reported that the bulk modulus obtained by hydrostatic compression testing of natural rubber was decreasing with reduced temperature. Thus, it is likely that the bulk modulus κ_B of FKM to some extent is temperature dependent. However, such a dependence would have limited influence on the simulation results presented herein.

5. Concluding remarks

An experimental procedure enabling measurement of the volume growth accompanying tension of elastomers at low temperatures was outlined. The use of grease and icing sugar to obtain the DIC speckle patterns was found to be superior over traditional spray painting for low temperature testing. The experiments on HNBR and FKM compounds provided novel data, showing a significant increase in the volume growth accompanying uniaxial tension as the temperature was reduced from 23 to -18 °C. By the use of in situ SEM, matrix-particle debonding was observed for two of the materials during tension at room temperature, yielding a micro-mechanical explanation for the macroscopically observed volume growth. The thermal sensitivity of the volumetric response of the materials can consequently be assumed to stem from a temperature dependence for the properties of the cohesive zone between the matrix material and filler particles.

A constitutive model capable of describing the experimentally observed effects was established by combining the Bergström-Boyce visco-hyperelastic elastomer model with the Gurson flow potential function to define the direction of the viscous flow. The proposed constitutive model was implemented as a user material for the finite element software LS-DYNA. Thermal features were

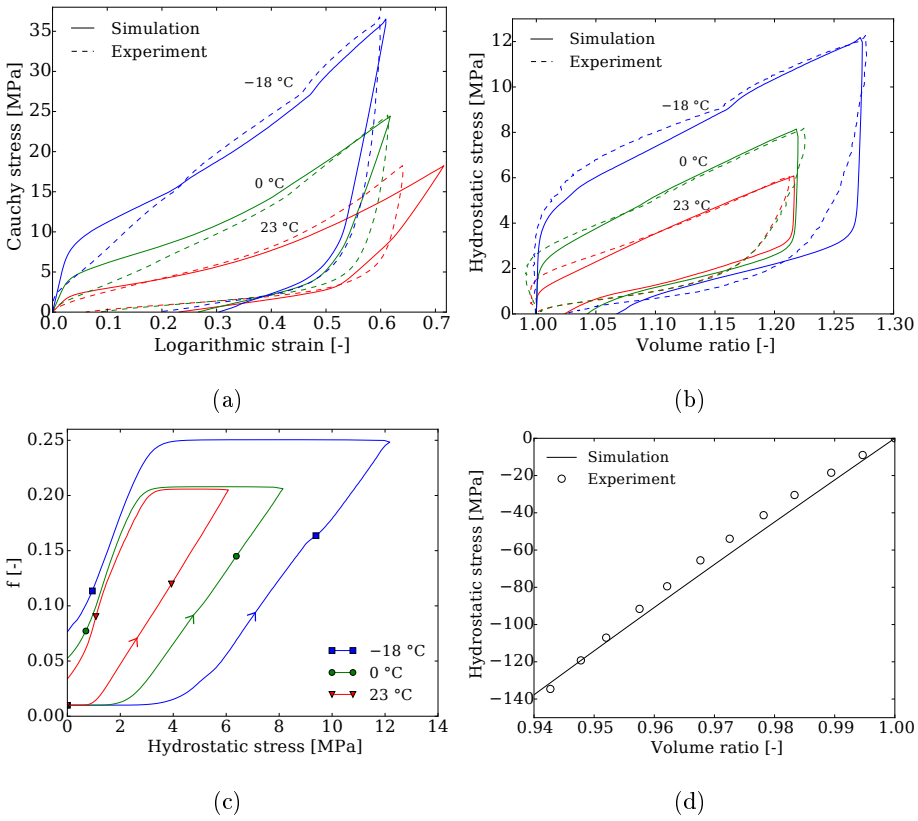

Figure 10: Simulation results from the proposed constitutive model, (a) Cauchy stress - logarithmic strain compared with FKM experimental data, (b) hydrostatic stress - volume ratio compared with FKM experimental data, (c) evolution of f during the simulations at each temperature, and (d) model behaviour during volumetric compression compared with experimental confined axial compression data for an FKM compound [8].

included in the model by defining a temperature dependent mathematical relation for five of the model parameters. With optimized input parameters, the model showed a good fit to the experimental data for both the stress - strain behaviour and the hydrostatic stress - volume ratio response at all three temperature levels. In addition, the model's response to a hydrostatic compression stress was seen to conform well to previously presented experimental results for confined axial compression.

Acknowledgements

The authors would like to acknowledge Aker Solutions AS for their funding of this research. In addition, we gratefully acknowledge Mr Trond Auestad for his assistance with the low temperature tension tests, Mr Christian Oen Paulsen for his assistance performing the SEM study, and Professor Odd Sture Hopperstad for discussions on the model formulation.

References

[1] ISO, 10423:2009 Petroleum and natural gas industries – Drilling and production equipment – Wellhead and christmas tree equipment, Tech. rep. (2009).

[2] A. N. Gent, B. Park, Failure processes in elastomers at or near a rigid spherical inclusion, Journal of Materials Science 19 (1984) 1947–1956.

[3] K. Cho, A. N. Gent, P. S. Lam, Internal fracture in an elastomer containing a rigid inclusion, Journal of Materials Science 22 (1987) 2899–2905.

[4] J. B. Le Cam, E. Toussaint, Volume Variation in Stretched Natural Rubber: Competition between Cavitation and Stress-Induced Crystallization, Macromolecules 41 (2008) 7579–7583.

[5] J.-B. Le Cam, E. Toussaint, Cyclic volume changes in rubber, Mechanics of Materials 41 (2009) 898–901.

[6] J. de Crevoisier, G. Besnard, Y. Merckel, H. Zhang, F. Vion-Loisel, J. Caillard, D. Berghezan, C. Creton, J. Diani, M. Brieu, F. Hild, S. Roux, Volume changes in a filled elastomer studied via digital image correlation, Polymer Testing 31 (2012) 663–670.

[7] S. Cantournet, K. Layouni, L. Laiarinandrasana, R. Piques, Experimental investigation and modelling of compressibility induced by damage in carbon black-reinforced natural rubber, Comptes Rendus Mécanique 342 (2014) 299–310.

[8] A. Ilseng, B. H. Skallerud, A. H. Clausen, An experimental and numerical study on the volume change of particle-filled elastomers in various loading modes, Mechanics of Materials 106 (2017) 44–57.

[9] A. Lion, On the large deformation behaviour of reinforced rubber at different temperatures, Journal of the Mechanics and Physics of Solids 45 (1997) 1805–1834.

[10] A. D. Drozdov, J. Christiansen, Thermo-viscoplasticity of carbon black-reinforced thermoplastic elastomers, International Journal of Solids and Structures 46 (2009) 2298–2308.

[11] H. Laurent, G. Rio, A. Vandenbroucke, N. Aït Hocine, H. L. G. Rio, A. V. N. Aït, Experimental and numerical study on the temperature-dependent behavior of a fluoro-elastomer, Mechanics of Time-Dependent Materials 18 (2014) 721–742.

[12] A. Ilseng, B. H. Skallerud, A. H. Clausen, Tension behaviour of HNBR and FKM elastomers for a wide range of temperatures, Polymer Testing 49 (2016) 128–136.

[13] R. S. Rivlin, Large Elastic Deformations of Isotropic Materials. IV. Further Developments of the General Theory, Philosophical Transactions of the Royal Society A: Mathematical, Physical and Engineering Sciences 241 (1948) 379–397.

[14] O. H. Yeoh, Some forms of the strain energy function for rubber, Rubber Chemistry and Technology 66 (1993) 754–771.

[15] R. W. Ogden, Large Deformation Isotropic Elasticity: On the Correlation of Theory and Experiment for Compressible Rubberlike Solids, Proceedings of the Royal Society of London A: Mathematical, Physical and Engineering Sciences 328 (1972) 567–583.

[16] E. M. Arruda, M. C. Boyce, A three-dimensional constitutive model for the large stretch behavior of rubber elastic materials, Journal of the Mechanics and Physics of Solids 41 (1993) 389–412.

[17] G. A. Holzapfel, J. C. Simo, A new viscoelastic constitutive model for continuous media at finite thermomechanical changes, International Journal of Solids and Structures 33 (1996) 3019–3034.

[18] A. Lion, A constitutive model for carbon black filled rubber: Experimental investigations and mathematical representation, Continuum Mechanics and Thermodynamics 8 (1996) 153–169.

[19] J. S. Bergström, M. C. Boyce, Constitutive modeling of the large strain time-dependent behavior of elastomers, Journal of the Mechanics and Physics of Solids 46 (1998) 931–954.

[20] G. Ayoub, F. Zaïri, M. Naït-Abdelaziz, J. Gloaguen, G. Kridli, A visco-hyperelastic damage model for cyclic stress-softening, hysteresis and permanent set in rubber using the network alteration theory, International Journal of Plasticity 54 (2014) 19–33.

[21] P. W. Bridgman, The Compression of Sixty-One Solid Substances to 25,000 kg/cm2 Determined by a New Rapid Method, Proceedings of the American Academy of Arts and Sciences 76 (1945) 9–24.

[22] L. A. Wood, G. M. Martin, Compressibility of Natural Rubber at Pressures Below 500 KG/CM2, Rubber Chemistry and Technology 37 (1964) 850–865.

[23] A. Ilseng, B. H. Skallerud, A. H. Clausen, Volumetric compression of HNBR and FKM elastomers, Constitutive Models for Rubber IX - Proceedings of the 9th European Conference on Constitutive Models for Rubbers, 2015, pp. 235–241.

[24] J. Li, D. Mayau, F. Song, A constitutive model for cavitation and cavity growth in rubber-like materials under arbitrary tri-axial loading, International Journal of Solids and Structures 44 (2007) 6080–6100.

[25] J. Li, D. Mayau, V. Lagarrigue, A constitutive model dealing with damage due to cavity growth and the Mullins effect in rubber-like materials under triaxial loading, Journal of the Mechanics and Physics of Solids 56 (2008) 953–973.

[26] O. Lopez-Pamies, T. Nakamura, M. I. Idiart, Cavitation in elastomeric solids: II - Onset-of-cavitation surfaces for Neo-Hookean materials, Journal of the Mechanics and Physics of Solids 59 (2011) 1488–1505.

[27] A. L. Gurson, Continuum Theory of Ductile Rupture by Void Nucleation and Growth: Part I-Yield Criteria and Flow Rules for Porous Ductile Media, Journal of Engineering Materials and Technology 99 (1977) 2–15.

[28] V. Tvergaard, Influence of voids on shear band instabilities under plane strain conditions, International Journal of Fracture 17 (1981) 389–407.

[29] B. Skallerud, Z. Zhang, A 3D numerical study of ductile tearing and fatigue crack growth under nominal cyclic plasticity, International journal of solids and structures 34 (1997) 3141–3161.

[30] Z. Zhang, C. Thaulow, J. Ødegård, A complete Gurson model approach for ductile fracture, Engineering Fracture Mechanics 67 (2000) 155–168.

[31] T. Pardoen, J. W. Hutchinson, Extended model for void growth and coalescence, Journal of the Mechanics and Physics of Solids 48 (2000) 2467–2512.

[32] J. Wen, Y. Huang, K. Hwang, C. Liu, M. Li, The modified Gurson model accounting for the void size effect, International Journal of Plasticity 21 (2005) 381–395.

[33] K. Nahshon, J. W. Hutchinson, Modification of the Gurson Model for shear failure, European Journal of Mechanics, A/Solids 27 (2008) 1–17.

[34] A. Steenbrink, E. Van Der Giessen, P. Wu, Void growth in glassy polymers, Journal of the Mechanics and Physics of Solids 45 (1997) 405–437.

[35] M. Challier, J. Besson, L. Laiarinandrasana, R. Piques, Damage and fracture of polyvinylidene fluoride (PVDF) at 20 C: Experiments and modelling, Engineering Fracture Mechanics 73 (2006) 79–90.

[36] T. F. Guo, J. Faleskog, C. F. Shih, Continuum modeling of a porous solid with pressure-sensitive dilatant matrix, Journal of the Mechanics and Physics of Solids 56 (2008) 2188–2212.

[37] ISO, 37:2011 Rubber, vulcanized or thermoplastic - Determination of tensile stress-strain properties, Tech. rep. (2011).

[38] J. Johnsen, F. Grytten, O. S. Hopperstad, A. H. Clausen, Experimental set-up for determination of the large-strain tensile behaviour of polymers at low temperatures, Polymer Testing 53 (2016) 305–313.

[39] E. Fagerholt, T. Børvik, O. Hopperstad, Measuring discontinuous displacement fields in cracked specimens using digital image correlation with mesh adaptation and crack-path optimization, Optics and Lasers in Engineering 51 (2013) 299–310.

[40] B. M. Patterson, N. L. Cordes, K. Henderson, J. J. Williams, T. Stannard, S. S. Singh, A. R. Ovejero, X. Xiao, M. Robinson, N. Chawla, In situ X-ray synchrotron tomographic imaging during the compression of hyper-elastic polymeric materials, Journal of Materials Science 51 (2016) 171–187.

[41] M. Karlsen, J. Hjelen, Ø. Grong, G. Rørvik, R. Chiron, U. Schubert, E. Nilsen, SEM/EBSD based in situ studies of deformation induced phase transformations in supermartensitic stainless steels, Materials Science and Technology 24 (2008) 64–72.

[42] J.-B. Le Cam, B. Huneau, E. Verron, L. Gornet, Mechanism of Fatigue Crack Growth in Carbon Black Filled Natural Rubber, Macromolecules 37 (2004) 5011–5017.

[43] B. Huneau, I. Masquelier, Y. Marco, V. Le Saux, S. Noizet, C. Schiel, P. Charrier, Initiation mechanisms of fatigue cracks in carbon black filled natural rubber, Constitutive Models for Rubber IX (2015) 395–401.

[44] G. A. Holzapfel, Nonlinear Solid Mechanics: A Continuum Approach for Engineering, John Wiley & Sons, 2000.

[45] T. Belytschko, W. K. Liu, B. Moran, K. Elkhodary, Nonlinear Finite Elements for Continua and Structures, Wiley, 2014.

[46] J. C. Simo, C. Miehe, Associative coupled thermoplasticity at finite strains: Formulation, numerical analysis and implementation, Computer Methods in Applied Mechanics and Engineering 98 (1992) 41–104.

[47] A. Cohen, A Padé approximant to the inverse Langevin function, Rheologica Acta 30 (1991) 270–273.

[48] F. Sidoroff, Un modèle viscoélastique non linéaire avec configuration intermédiaire, Journal de Mécanique 13 (1974) 679–713.

[49] J. Bergström, Mechanics of Solid Polymers, Elsevier, 2015.

[50] S. C. H. Lu, K. S. Pister, Decomposition of deformation and representation of the free energy function for isotropic thermoelastic solids, International Journal of Solids and Structures 11 (1975) 927–934.

[51] J. Bergström, L. Hilbert, A constitutive model for predicting the large deformation thermomechanical behavior of fluoropolymers, Mechanics of Materials 37 (2005) 899–913.

[52] G. Holzapfel, J. Simo, Entropy elasticity of isotropic rubber-like solids at finite strains, Computer Methods in Applied Mechanics and Engineering 132 (1996) 17–44.

[53] Livermore Software Technology Corporation (LSTC), LS-OPT User's Manual, version 5.2, 2015.

[54] Livermore Software Technology Corporation (LSTC), LS-DYNA keyword user's manual, version R8.0, vols 1 and 2, 2016.